

Design of the shell-infill structures using a phase field-based topology optimization method

Wenxuan Xie^a, Jiachen Feng^a, Qing Xia^a, Junseok Kim^b, Yibao Li^{a,*}

^a School of Mathematics and Statistics, Xi'an Jiaotong University, Xi'an 710049, China

^b Department of Mathematics, Korea University, Seoul 02841, Republic of Korea

ARTICLE INFO

Keywords:

Shell-infill structures
Porous infill architecture
Phase field method
Multiscale topology optimization

ABSTRACT

The design of shell-infill structures has been a focal point in the topology optimization community due to their advantages in energy absorption characteristics, strength-to weight ratio and bucking resistance. This paper introduces a phase field-based topology optimization method for designing shell-infill structures. Interface-related issues can be easily addressed through the phase field function. A coupled topology optimization process is proposed to establish the connection between the shell and infill, facilitating the generation of optimized structures. The shell thickness, infill pattern and infill volume percentage, can be naturally controlled by different model parameters. Additionally, multiscale phase field topology optimization integrates the numerical homogenization method to evaluate the effective elasticity matrix of the microstructural infill. The approach is introduced for a uniform, periodical microstructure layout in the infill region, thereby achieving superior mechanical properties. Numerical results indicate the effectiveness of the proposed method in the design of both 2D and 3D shell-infill structures.

1. Introduction

Shell-infill structures [1–3] are widely observed in nature, such as human bones, bird beaks and plant stems. Drawing inspiration from these bio-structures, the shell-infill structures have become a prominent focus in additive manufacturing, coated implants and architectures. Typically, such type of structure is composed of an inner portion of porous infill and a solid outer shell [4–6]. The shell can be regarded as an external wall, playing a crucial role in maintaining the overall structure. The internal infill, which is designed to a porous structure, serves to preserve the structural strength. In contrast to solid bulky counterparts that are even topology-optimized, shell-infill structures have garnered considerable attention due to their advantageous properties in energy absorption characteristics [7], strength-to weight ratio and bucking resistance [8].

In the design of shell-infill structure, achieving the optimal structure with the best matching between the geometry of the shells and the topology of the infills is a challenging problem. A pertinent way to design shell-infill structures is based on the structural Topology Optimization [9,10], which is considered as a powerful method to design lightweight structures with optimized mechanical properties. The density-based topology optimization method represented by SIMP (Solid Isotropic Material with Penalization) method was successfully applied in the design of shell-infill structures [11]. Based on the Clausen's coated approach [12,13], Wu et al. [14] developed a concurrent topology optimization method for evolving the shell and non-uniform infill architecture. Inspired by the architecture of bone, Wu et al. [15] presented a SIMP-based approach for the generation of bone-like porous structures. Zhou

* Corresponding author.

E-mail address: yibaoli@xjtu.edu.cn (Y. Li).

URL: <http://gr.xjtu.edu.cn/web/yibaoli> (Y. Li).

et al. [16] extended Wu's work for shells with self-supporting infills. Based on the idea of erosion interface identification method, Luo et al. [17] presented an improved SIMP method for shell-infill structures. Furthermore, Qiu et al. [18] proposed an evolutionary design approach for shell-infill structures that could control the infill architecture flexibly through the bi-directional evolutionary structural optimization method [19].

Due to the advantages of simplicity, the density method has great success in the design of shell-infill structures. However, challenges arise in the application of these density-based approaches, giving rise to non-physical numerical instabilities, notably checkerboard patterns, grayscales, and mesh dependency [20]. Moreover, a crucial concern in the design of shell-infill structures pertains to the identification of the material interface, which is often regarded as a difficulty of density based approaches [12,17]. Compared with the material density-based approach relying on multi-step projections, the boundary variation topology optimization method can give a more direct and accurate description of the material interface and the geometrical information including the boundary normal directions and the coating thickness. Wang and Kang [21] firstly utilized a level set function to describe the shell and infill, afterwards the level set method is applied to optimize coated structures. Bai et al. [22] utilized the multi-material level set method to design the coated structures for better performances. One primary problem with the level set method is the necessity and difficulty in the re-initialization, which results in extra re-initialization error and conservation error [23,24]. The phase field topology optimization method [25–28], which is also regarded as a representative boundary variation methods, is an alternative methods for rectifying these problems. Similar to the level set method, the phase field method can track the complex interface implicitly. The structural topology optimization problem is regarded as a phase transition problem which is described by a phase-field function. The function varies sharply across the interface between different phased, while the interface holds a thickness [29,30]. This makes the identification of the material interface become flexible and accurate.

Most of the attention in current studies aims to the shell-infill structures in single scale. The overall mechanical properties of the structures are kept away from the optimal performance when only single scale topology optimization is considered, since the shell and infill are processed as separate materials [31]. The multiscale topology optimization [32–36] has become an effective and important mechanical design tool for engineering applications, which can achieve advantage properties of the composite structure. To comprehensively explore the attributes and performance of shell-infill structures, there is a necessity to enhance the design methodology from a mono-scale approach to a multiscale topology optimization method. Fu et al. [31] firstly proposed a multiscale topology optimization method for the shell-infill structures based on the level set method. Wadbro and Niu [37] considered a SIMP-base multiscale topology optimization of the infill structures. Xu et al. [38] extended the variable thickness sheet multiscale topology optimization method for lattice structure design with both shell and lattice–lattice interface layers to enhance the structural mechanical properties and manufacturability. A systematic multiscale topology optimization method based on the phase field method was proposed in [39]. With this fundamental work, we aim to utilize the phase field multiscale topology optimization method for the design of shell-infill structures.

This paper provides a novel, phase field-based framework to study the shape and topology optimization problem of coated structures at both single and multi scales. The representation of shell and infill region is naturally handled by a phase field function, enabling the easy identification of interfaces. Afterwards, the optimal shell layout and infill pattern are determined using a coupled topology optimization method. Critical indicators in the shell-infill composites, including the shell thickness, infill pattern and infill volume percentage, can be directly and simply controlled by three parameters. Furthermore, the microscopic pattern of the infill region can be determined by the multiscale topology optimization method, in which the numerical homogenization facilitates the analysis of the connection between microstructures and the macroscopic properties of the infill material. Due to the presence of numerous coexisting microstructures, the mechanical performance of the optimized two-scale structural design can be significantly enhanced. In order to demonstrate the effectiveness of the proposed method, we carried out a series of experiments in both two- and three-dimensional space. To the best of our knowledge, this study is the first paper to investigate the design of shell-infill structures through the single and multi scales phase field topology optimization method.

The remainder of this paper is organized as follows. In Section 2, the phase field-based framework for the shell-infill structures is established in both single and multi scales. In Section 3, the numerical schemes for different evolved equations are proposed. The effectiveness and practicability of the present method are verified through several numerical experiments in Section 4. Some concluding remarks are given in Section 5.

2. Shell-infill optimization

Topology optimization achieves the design of advanced structures with improved and required physical properties by optimizing the distribution of material under a series of constraints. In this section, we establish a novel topology optimization framework for shell-infill structures based on the phase field method. We take a typical compliance minimization problem as an example here.

2.1. Phase field topology optimization method

In the framework of phase field method [40–42], the design domain Ω is described by a phase field function $\phi(\mathbf{x})$

$$\begin{cases} \phi(\mathbf{x}) = 0, & \mathbf{x} \in \Omega_0, \\ 0 < \phi(\mathbf{x}) < 1, & \mathbf{x} \in \Omega \setminus (\Omega_0 \cup \Omega_1), \\ \phi(\mathbf{x}) = 1, & \mathbf{x} \in \Omega_1. \end{cases} \quad (1)$$

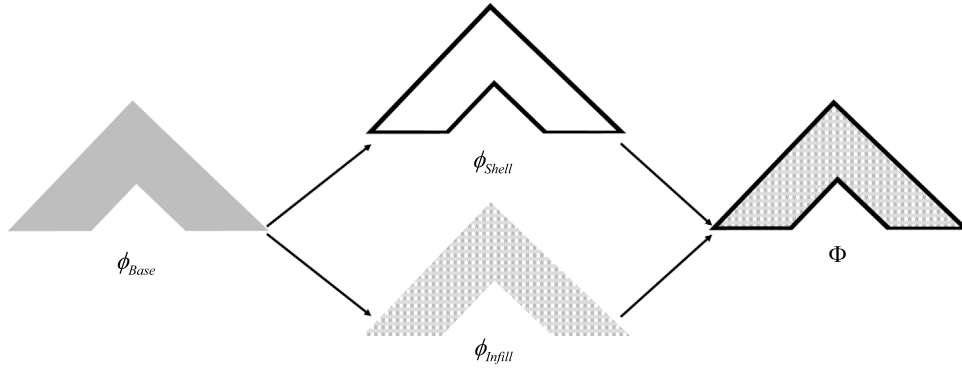


Fig. 1. The conceptual composition of the present topology optimization framework for shell-infill structures.

The function $\phi(\mathbf{x})$ divides Ω into the void region Ω_0 , the solid region Ω_1 and the interface diffuse region $\Omega \setminus (\Omega_0 \cup \Omega_1)$. The diffusive interface holds the thickness ϵ .

In the problem of compliance minimization, the objective function and the constraints are established as follows:

$$\min : \quad J(\phi, \mathbf{u}) = \int_{\Omega} W(\phi, \mathbf{u}) d\mathbf{x}, \tag{2}$$

$$\text{subject to :} \quad \begin{cases} \nabla \cdot g(\phi)\sigma^0 = \mathbf{0}, \\ V(\phi) = V_0, \\ 0 \leq \phi \leq 1. \end{cases} \tag{3}$$

Here $\mathbf{u} = (u, v)$ is the displacement. $W(\phi, \mathbf{u})$ represents the function of local elastic strain density, which is formulated by $W(\phi, \mathbf{u}) = (\boldsymbol{\epsilon}(\mathbf{u}) : \mathbf{D}(\phi) : \boldsymbol{\epsilon}(\mathbf{u}))/2$. σ^0 is the Cauchy stress tensor, $g(\phi) = g_{min} + (1 - g_{min})\phi^3$ is the interpolation function where g_{min} is a small positive value. Set $\mathbf{D}(\phi) = g(\phi)\mathbf{D}^0$, in which the fourth-order stiffness tensor is written as $D_{ijkl}^0 = 2G(\delta_{ik}\delta_{jl} + \frac{\nu}{1-2\nu}\delta_{ij}\delta_{kl})$. The shear modulus is represented as $G = E/2(1 + \nu)$, in which E and ν are the elasticity modulus and Poisson's ratio respectively. δ is the Kronecker delta function. $V(\phi) = \int_{\Omega} \phi d\mathbf{x}$, V_0 is the constrained volume fraction. In elastostatics, the linear elastic boundary value problem, which considers the coupling relationship of displacement, strain and stress is characterized by the equilibrium equation, constitutive equation and strain–displacement equation [29]:

$$\begin{cases} \nabla \cdot g(\phi)\sigma^0 = \mathbf{0}, \\ \sigma^0 = \mathbf{D}^0 : \boldsymbol{\epsilon}(\mathbf{u}), \\ \boldsymbol{\epsilon}(\mathbf{u}) = \frac{1}{2}(\nabla\mathbf{u} + (\nabla\mathbf{u})^T). \end{cases} \tag{4}$$

In order to obtain the based design of the shell-infill structures, we establish a modified energy function $E(\phi, \mathbf{u})$ by the principle of virtual work:

$$\min : \quad E(\phi, \mathbf{u}) = \eta \int_{\Omega} W(\phi, \mathbf{u}) d\mathbf{x} + \int_{\Omega} \left(\frac{\epsilon^2}{2} |\nabla\phi|^2 + F(\phi) \right) d\mathbf{x} + \frac{\beta}{2} (V(\phi) - V_0)^2, \tag{5}$$

Here $F(\phi) = 0.25\phi^2(1 - \phi)^2$ represents the double well potential. η and β are positive constant parameters.

2.2. Representation of shell and infill structures

Fig. 1 demonstrates the conceptual composition of our topology optimization framework for shell-infill structures. First, an optimal material distribution ϕ_{Base} is obtained by solving the original compliance minimization problem Eqs. (4) and (5). Second, ϕ_{Base} is used as a based design variable to generate the shell region ϕ_{Shell} and the infill region ϕ_{Infill} . Third, a topology optimization process coupled with the shell region is performed to optimize the infill region, then the porous infill can be obtained. Furthermore, the microstructure of the infill region can be controlled by the multiscale phase field topology optimization method. Finally, the optimized shell-infill structure Φ is obtained by combining ϕ_{Shell} and ϕ_{Infill} through an interpolation function.

We consider a rectangular design domain Ω with width L_x and length L_y , which is discretized by a uniform mesh with length h . Here $h = L_x/N_x = L_y/N_y$ is defined. The center of each element is located at $\mathbf{x}_{ij} = (x_i, y_j) = ((i-0.5)h, (j-0.5)h)$, where $i = 1, \dots, N_x$ and $j = 1, \dots, N_y$. Assuming that the based design variable ϕ_{Base} has been obtained on design domain Ω . If $0 < \phi_{Base}(x_i, y_j) - 0.1 < 0.2$, $\phi_{Shell}(x_{i\pm r_N}, y_{j\pm r_N})$ is set to $\phi_{Base}(x_{i\pm r_N}, y_{j\pm r_N})$, and $\phi_{Shell} = 0$ at other points on Ω . Here r_N is a positive integer which is used to control the thickness of the shell. If $\phi_{Shell}(x_i, y_j) = 0$ and $\phi_{Base}(x_i, y_j) - 0.1 > 0$, $\phi_{Infill}(x_i, y_j)$ is set to 1, and $\phi_{Infill} = 0$ at other points on Ω . Fig. 2 illustrates an example for ϕ_{Base} , ϕ_{Shell} and ϕ_{Infill} with shell thickness $r_N = 1$.

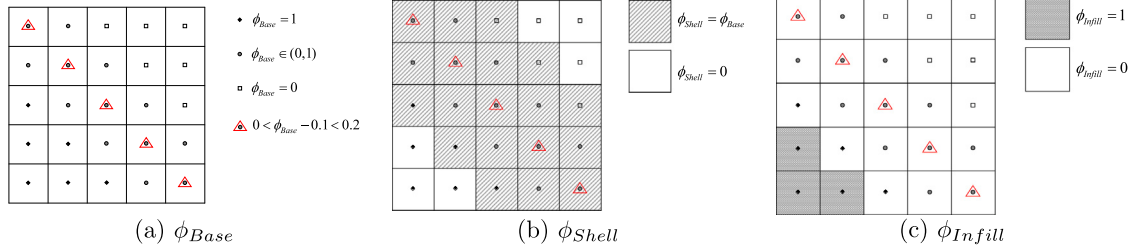


Fig. 2. An example for ϕ_{Base} , ϕ_{Shell} and ϕ_{Infill} with shell thickness $r_N = 1$.

2.3. Topology optimization for the infill region

It is expected that the infill region is composed of porous structures. An additional topology optimization process is necessary to obtain the optimized infill design, in which the shell region is fixed and the optimization of ϕ_{Infill} is coupled with ϕ_{Shell} . The modified energy function of the coupled topology optimization is given as:

$$\begin{aligned} \min : E(\phi_{Infill}, \mathbf{u}) = & \eta \int_{\Omega} W(\phi_{Infill}, \mathbf{u}) d\mathbf{x} + \int_{\Omega} \left(\frac{\epsilon^2}{2} |\nabla \phi_{Infill}|^2 + F(\phi_{Infill}) \right) d\mathbf{x} \\ & + \frac{\beta}{2} \left(V(\phi_{Infill}) - V_1 \right)^2, \end{aligned} \tag{6}$$

with the modified linear elastic boundary value problem:

$$\begin{cases} \nabla \cdot \tilde{g}(\phi_{Shell}, \phi_{Infill}) \boldsymbol{\sigma}^0(\mathbf{u}) = \mathbf{0}, \\ \tilde{g}(\phi_{Shell}, \phi_{Infill}) = g_{min} + (1 - g_{min}) \tilde{\phi}^3 \\ \tilde{\phi} = \max(\phi_{Shell}, g_1 \phi_{Infill}). \end{cases} \tag{7}$$

Here $W(\phi_{Infill}, \mathbf{u}) = (\boldsymbol{\epsilon}(\mathbf{u}) : \mathbf{g}(\phi_{Infill}) \mathbf{D}^0 : \boldsymbol{\epsilon}(\mathbf{u})) / 2$, V_1 is the constrained volume fraction for the infill region, g_1 is the parameter that controls the material properties of the infill region. Both V_1 and g_1 are applied to control the porous structures. We note that ϕ_{Infill} is optimized through Eqs. (6), and the optimization of ϕ_{Infill} is coupled with the fixed shell by $\tilde{\phi}$. When the optimized infill structure is obtained, ϕ_{Shell} and ϕ_{Infill} are combined to generate the final structure Φ , which is defined through the following interpolation function:

$$\Phi(\phi_{Base}, \phi_{Shell}, \phi_{Infill}) = \phi_{Base} \phi_{Infill} + (1 - \phi_{Base} \phi_{Infill}) \phi_{Shell}. \tag{8}$$

Here, the interpolation way can guarantee that Φ has values in the interval [0, 1].

2.4. Multiscale design model for infill structures

In this section, we assume that the infill region comprises microstructures that are periodically distributed. The phase field multiscale topology optimization method is utilized to achieve the design of infill region with different pattern of the microstructures. The size of the microstructures are significantly smaller than those of the macro structures. Therefore the design domain, the structure boundaries and the relevant variables need to be distinguished as macro and micro. The global coordinate system \mathbf{x} and the local coordinate system \mathbf{y} are applied to depict the position of macrostructure and microstructure respectively. We use different superscript A and I to represent the macro-scale quantities and micro-scale quantities.

Consider the macro and micro design domain Ω^A and Ω^I , which are discretized into N^A and N^I elements respectively. ϕ_i^A and ϕ_j^I represent the phase field function of the i th and j th elements in Ω^A and Ω^I . The mathematical equation of phase field multiscale topology optimization for the infill region is provided as follows:

$$\begin{aligned} \text{find : } & \phi_i^A, \phi_j^I \quad (i = 1, \dots, N^A; j = 1, \dots, N^I) \\ \text{min : } & E^*(\phi^A, \phi^I) = \eta^A \int_{\Omega^A} \boldsymbol{\epsilon}(\mathbf{u}^A) : \mathbf{g}(\phi^A) \mathbf{D}^H : \boldsymbol{\epsilon}(\mathbf{u}^A) d\mathbf{x} + \int_{\Omega^A} \left(\frac{(\epsilon^A)^2}{2} |\nabla \phi^A|^2 + F(\phi^A) \right) d\mathbf{x} \\ & + \frac{\beta^A}{2} \left(V(\phi^A) - V_1^A \right)^2. \end{aligned}$$

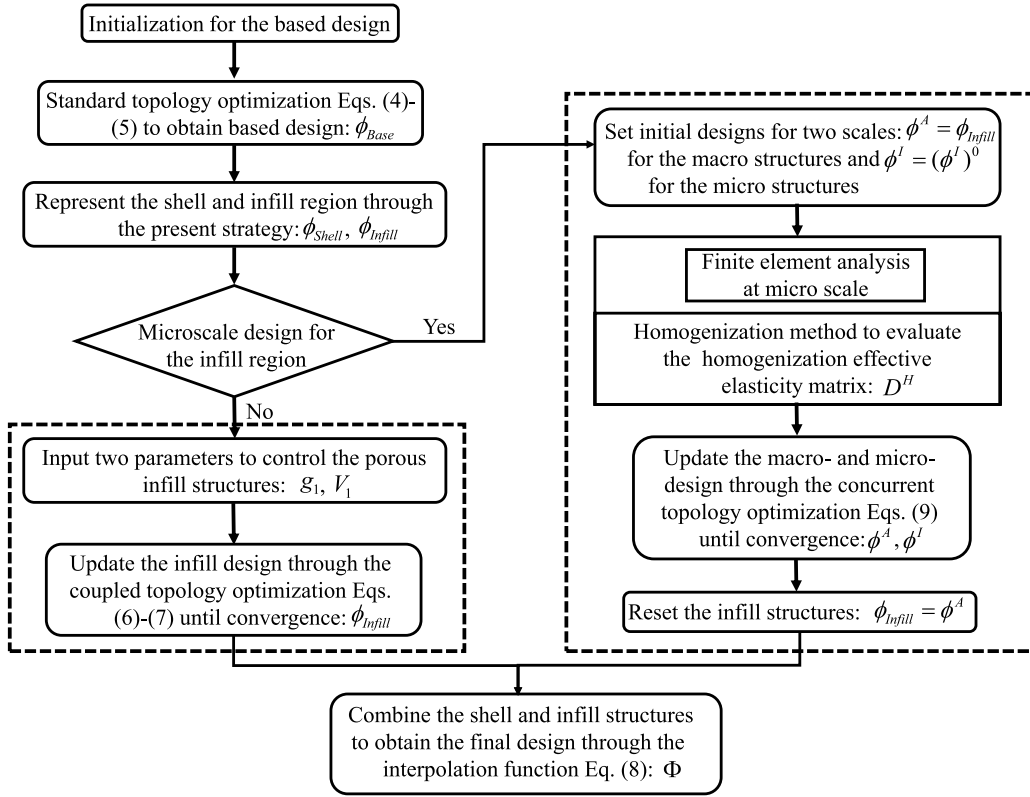


Fig. 3. Flowchart of phase-field based topology optimization of shell-infill structures.

$$\begin{cases} \int_{\Omega^A} \varepsilon(\mathbf{u}^A) : \tilde{g}(\phi_{Shell}, \phi^A) \mathbf{D}^H : \varepsilon(\mathbf{v}^A) d\mathbf{x} = \int_{\partial\Omega^A} \mathbf{s} \cdot \mathbf{v}^A ds, & \forall \mathbf{v}^A \in \mathbf{V}(\Omega^A), \quad \forall \mathbf{v}^A \in \mathbf{V}(\Omega^A), \\ \int_{\Omega^I} \varepsilon(\mathbf{u}^I) : g(\phi^I) \mathbf{D}^I : \varepsilon(\mathbf{v}^I) d\mathbf{y} = \int_{\Omega^I} \varepsilon(\mathbf{u}^0) : g(\phi^I) \mathbf{D}^I : \varepsilon(\mathbf{v}^I) d\mathbf{y}, & \forall \mathbf{v}^I \in \mathbf{V}(\Omega^I), \\ \mathbf{D}^H = \frac{1}{|\Omega^I|} \int_{\Omega^I} (\varepsilon(\mathbf{u}^0) - \varepsilon(\mathbf{u}^I)) : g(\phi^I) \mathbf{D}^I : (\varepsilon(\mathbf{u}^0) - \varepsilon(\mathbf{u}^I)) d\mathbf{y}, \\ \int_{\Omega^I} \phi^I d\mathbf{y} \leq V^I = \frac{1}{N^A} \sum_{i=1}^{N^A} \phi_i^A. \end{cases} \quad (9)$$

Multiscale topology optimization method targets in finding the optimal distribution of ϕ^A and ϕ^I , minimizing the compliance of the macrostructure within the infill region. \mathbf{u}^A and \mathbf{u}^I represent the displacement of macro and micro elements in Ω^A and Ω^I , while $\varepsilon(\mathbf{u}^0)$ indicates the linearly independent unit test strain field. $\mathbf{D}^I = \mathbf{D}^0$ is the fourth-order stiffness tensor. The homogenized stiffness tensor \mathbf{D}^H is given by averaging the integral over the micro elements Ω^I , in which the homogenization method is applied to evaluate the macroscopic effective properties. In order to enhance the effectiveness of current algorithms in topology optimization, \mathbf{D}^H can be reformulated equivalently using element mutual energies [43,44]:

$$\mathbf{D}_{ijkl}^H = \frac{1}{|\Omega^I|} \int_{\Omega^I} (\varepsilon_{pq}(\mathbf{u}^{0(ij)}) - \varepsilon_{pq}(\mathbf{u}^{I(ij)})) g(\phi^I) \mathbf{D}_{pqrs}^I (\varepsilon_{rs}(\mathbf{u}^{0(kl)}) - \varepsilon_{rs}(\mathbf{u}^{I(kl)})) d\mathbf{y}.$$

Here \mathbf{V} is the kinematically admissible displacement space, \mathbf{v}^A and \mathbf{v}^I are the virtual displacement field in macroscale and microscale. $|\Omega^I|$ represents the area of the micro design domain Ω^I . V^I is the microstructure volume constraint, which is controlled by the regularized density.

The optimal distribution of ϕ^A , which is composed of porous and uniform microstructures, can be obtained by solving the optimization problem Eqs. (9). Furthermore the infill region ϕ_{Infill} is set to ϕ^A and the final structure Φ can be generated by Eq. (8).

The flowchart of our proposed phase-field based topology optimization method for the shell-infill structures is illustrated in Fig. 3, while a specific example of the proposed method is given in Fig. 4.

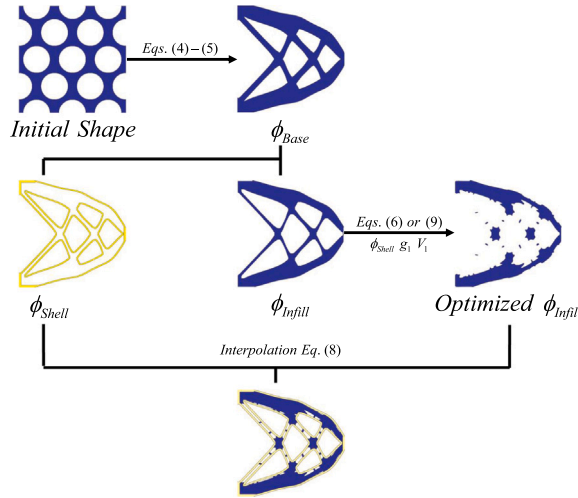


Fig. 4. The general idea and a specific example of the proposed phase-field based topology optimization method for shell-infill structures.

3. Numerical implementation

For the compliance minimization problem Eqs. (4) and (5), a phase field evolution equation can be derived through the principle of gradient flow of the energy Eq. (5) [45–47]. ϕ_t is proportional to the negative gradient of $E(\phi, \mathbf{u})$:

$$\begin{aligned} \phi_t &= -\frac{\partial E(\phi, \mathbf{u})}{\partial \phi} = -\eta \frac{\partial W}{\partial \phi} + \epsilon^2 (\nabla^2 \phi - \frac{F'(\phi)}{\epsilon^2}) - \beta (V(\phi) - V_0), \\ \frac{\partial W}{\partial \phi} &= \frac{1}{2} \epsilon(\mathbf{u}) : 3\phi^2 \mathbf{D}^0 : \epsilon(\mathbf{u}). \end{aligned} \tag{10}$$

The boundary condition for ϕ is set to $\mathbf{n} \cdot \nabla \phi = 0$.

A hybrid numerical method based on the finite element method and the finite difference method is proposed to give the numerical schemes. Here Δt is the time step, $\phi_{i,j}^n$ represents the approximation of $\phi(x_{i,j})$ at time $n\Delta t$. The displacement field \mathbf{u}^{n+1} is first updated by solving the linear elastic problem using the finite element method:

$$\nabla \cdot (g(\phi^n) \mathbf{D}^0 : \epsilon(\mathbf{u}^{n+1})) = \mathbf{0}, \tag{11}$$

with the boundary conditions:

$$\begin{cases} \mathbf{u}^{n+1} = \mathbf{0}, & \text{on } \Gamma_1 \subset \partial\Omega, \\ \mathbf{n} \cdot \sigma(\phi^n, \mathbf{u}^{n+1}) = \mathbf{s}, & \text{on } \Gamma_2 \subset \partial\Omega, \\ \mathbf{n} \cdot \sigma(\phi^n, \mathbf{u}^{n+1}) = \mathbf{0}, & \text{on } \partial\Omega / (\Gamma_1 \cup \Gamma_2). \end{cases} \tag{12}$$

The finite difference method is applied to solve the phase field evolution function Eq. (10). The Crank–Nicolson style scheme is considered:

$$\begin{aligned} \frac{\phi^{n+1} - \phi^n}{\Delta t} &= -\eta \frac{\omega(\phi^{n+1}, \mathbf{u}^{n+1}) + \omega(\phi^n, \mathbf{u}^n)}{2} - (F'(\check{\phi}^{n+\frac{1}{2}}) - \epsilon^2 \Delta_d \phi^{n+\frac{1}{2}} - \lambda \check{\phi}^{n+\frac{1}{2}} + \lambda \phi^{n+\frac{1}{2}}) \\ &\quad - \beta \left(\frac{V_d(\phi^{n+1}) + V_d(\phi^n)}{2} - V_0 \right), \end{aligned} \tag{13}$$

where $\omega(\phi^n, \mathbf{u}^n) = \partial W(\phi^n, \mathbf{u}^n) / \partial \phi^n = (\epsilon(\mathbf{u}^n) : 3(\phi^n)^2 \mathbf{D}^0 : \epsilon(\mathbf{u}^n)) / 2$, $\check{\phi}^{n+\frac{1}{2}} = (3\phi^n - \phi^{n-1}) / 2$, $\phi^{n+\frac{1}{2}} = (\phi^n + \phi^{n+1}) / 2$, λ is a stabilizing parameter, Δ_d is the discrete five point Laplacian operator, $V_d(\phi^n) = h^2 \sum_{i=1}^{N_x} \sum_{j=1}^{N_y} \phi_{i,j}^n$ is the discrete volume operator. Here the numerical scheme is solved by the nonlinear full approximation storage (FAS) multigrid method. The nonlinearity term is treated by one step of Newton’s iteration. We propose a pointwise Gauss–Seidel relaxation scheme as the smoother in the multigrid method:

$$\begin{aligned} &\left(\frac{1}{\Delta t} + \frac{2\epsilon^2}{h^2} + \frac{\lambda}{2} + \frac{\beta h^2}{2} + \frac{\eta}{2} \frac{d\omega(\phi_{ij}^m, \mathbf{u}_{ij}^{n+1})}{d\phi} \right) \phi_{ij}^{m+1} \\ &= \frac{1}{\Delta t} \phi_{ij}^n - \frac{\eta}{2} \omega(\phi_{ij}^m, \mathbf{u}_{ij}^{n+1}) + \frac{\eta}{2} \frac{d\omega(\phi_{ij}^m, \mathbf{u}_{ij}^{n+1})}{d\phi} \phi_{ij}^m - \frac{\eta}{2} \omega(\phi_{ij}^n, \mathbf{u}_{ij}^n) \end{aligned}$$

$$\begin{aligned}
 & - (F'(\check{\phi}_{ij}^{n+\frac{1}{2}}) - \frac{\epsilon^2}{2} \frac{\phi_{i-1,j}^{m+1} + \phi_{i,j-1}^{m+1} + \phi_{i+1,j}^m + \phi_{i,j+1}^m}{h^2} - \frac{\epsilon^2}{2} \frac{\phi_{i-1,j}^n + \phi_{i,j-1}^n + \phi_{i+1,j}^n + \phi_{i,j+1}^n - 4\phi_{i,j}^n}{h^2}) \\
 & - \lambda \check{\phi}_{ij}^{n+\frac{1}{2}} + \frac{\lambda}{2} \phi_{ij}^n - \beta (\frac{h^2}{2} \sum_{\substack{k \leq i, l \leq j \\ (k,l) \neq (i,j)}} \phi_{i,j}^{m+1} + \frac{h^2}{2} \sum_{\substack{k \geq i, l \geq j \\ (k,l) \neq (i,j)}} \phi_{i,j}^m + \frac{V_d(\phi^n)}{2} - V_0),
 \end{aligned}$$

Here $\phi_{i,j}^{m+1}$ and $\phi_{i,j}^m$ represent the approximations of $\phi_{i,j}^{n+1}$ before and after a step of relaxation operator. We note that the nonlinear term $\omega(\phi^{m+1}, \mathbf{u}^{n+1})$ can be linearized at ϕ_{ij}^m by $\omega(\phi^{m+1}, \mathbf{u}^{n+1}) = \omega(\phi^m, \mathbf{u}^{n+1}) + \frac{d\omega(\phi_{ij}^m, \mathbf{u}_{ij}^{n+1})}{d\phi} (\phi_{ij}^{m+1} - \phi_{ij}^m)$. When $\|\phi^{m+1} - \phi^m\|_{L^2} < tol$, then we set $\phi^{n+1} = \phi^{m+1}$. The tolerance is set to $tol = 1e - 5$. For more details about the FAS multigrid method, please refer to [48,49].

Next the numerical scheme for the multiscale topology optimization problem Eqs. (9) is considered. Similarly to the standard topology optimization problem, we can derive the evolution equation for the macroscale and microscale phase field function ϕ^A and ϕ^I respectively:

$$\begin{cases} \phi_t^A = -\eta^A \frac{\partial W^A}{\partial \phi^A} + (\epsilon^A)^2 (\nabla^2 \phi^A - \frac{F'(\phi^A)}{(\epsilon^A)^2}) - \beta^A (V(\phi^A) - V_1^A), \\ \phi_t^I = -\eta^I \frac{\partial W^A}{\partial \phi^I} + (\epsilon^I)^2 (\nabla^2 \phi^I - \frac{F'(\phi^I)}{(\epsilon^I)^2}) - \beta^I (V(\phi^I) - V^I), \end{cases} \tag{14}$$

We note that the local elastic strain energy density for the macroscale holds the form $W^A = \epsilon(\mathbf{u}^A) : (\phi^A)^3 \mathbf{D}^H : \epsilon(\mathbf{u}^A) d\mathbf{x}/2$, in which the standard stiffness tensor \mathbf{D}^0 is replaced by the homogenization stiffness tensor \mathbf{D}^H . In other words, W^A is coupled with both macroscale design variables ϕ^A and microscale design variables ϕ^I . The first-order derivatives of W^A with respect to ϕ^A and ϕ^I in Eqs. (14) can be expressed as follows:

$$\begin{cases} \frac{\partial W^A}{\partial \phi^A} = -\frac{1}{2} \epsilon(\mathbf{u}^A) : (3(\phi^A)^2) \mathbf{D}^H : \epsilon(\mathbf{u}^A), \\ \frac{\partial W^A}{\partial \phi^I} = -\frac{1}{2} \epsilon(\mathbf{u}^A) : (\phi^A)^3 \frac{\partial \mathbf{D}^H}{\partial \phi^I} : \epsilon(\mathbf{u}^A), \\ \frac{\partial \mathbf{D}^H}{\partial \phi^I} = \frac{1}{|\Omega^I|} \int_{\Omega^I} (\epsilon(\mathbf{u}^0) - \epsilon(\mathbf{u}^I)) : (3(\phi^I)^2) \mathbf{D}^I : (\epsilon(\mathbf{u}^0) - \epsilon(\mathbf{u}^I)) d\mathbf{y}. \end{cases} \tag{15}$$

The macro design domain $\Omega^A = (0, L_x^A) \times (0, L_y^A)$ and the micro design domain $\Omega^I = (0, L_x^I) \times (0, L_y^I)$ are discretized using separate uniform mesh. For macro design domain, the $N_x^A \times N_y^A$ mesh with $h^A = L_x^A/N_x^A = L_y^A/N_y^A$ is applied, here the center of macro grid is defined at $\mathbf{x}_{ij} = (x_i, y_j) = ((i - 0.5)h^A, (j - 0.5)h^A)$. Similarly, the micro design domain is discretized by the $N_x^I \times N_y^I$ mesh with $h^I = L_x^I/N_x^I = L_y^I/N_y^I$, and the center of micro grid is defined at $\mathbf{y}_{ij} = (x_i, y_j) = ((i - 0.5)h^I, (j - 0.5)h^I)$. The time step for macroscale and microscale are defined as Δt^A and Δt^I respectively, and the approximation of $\phi^A(\mathbf{x}_{ij}, n\Delta t^A)$ and $\phi^I(\mathbf{y}_{ij}, n\Delta t^I)$ are indicated as $(\phi^A)_{ij}^n$ and $(\phi^I)_{ij}^n$. Similar to the Crank–Nicolson scheme Eq. (13) for standard topology optimization problem, the numerical scheme for Eqs. (14) is derived as follows:

$$\begin{cases} \frac{(\phi^A)^{n+1} - (\phi^A)^n}{\Delta t^A} = -\eta^A \frac{(\omega^A)^{n+1} + (\omega^A)^n}{2} - (F'((\check{\phi}^A)^{n+\frac{1}{2}}) - (\epsilon^A)^2 \Delta_d (\phi^A)^{n+\frac{1}{2}} - \lambda(\check{\phi}^A)^{n+\frac{1}{2}} + \lambda(\phi^A)^{n+\frac{1}{2}}) \\ \quad - \beta^A \left(\frac{V_d((\phi^A)^{n+1}) + V_d((\phi^A)^n)}{2} - V_1^A \right), \\ \frac{(\phi^I)^{n+1} - (\phi^I)^n}{\Delta t^I} = -\eta^I \frac{(\omega^I)^{n+1} + (\omega^I)^n}{2} - (F'((\check{\phi}^I)^{n+\frac{1}{2}}) - (\epsilon^I)^2 \Delta_d (\phi^I)^{n+\frac{1}{2}} - \lambda(\check{\phi}^I)^{n+\frac{1}{2}} + \lambda(\phi^I)^{n+\frac{1}{2}}) \\ \quad - \beta^I \left(\frac{V_d((\phi^I)^{n+1}) + V_d((\phi^I)^n)}{2} - V^I \right). \end{cases} \tag{16}$$

and

$$\begin{cases} (\check{\phi}^A)^{n+\frac{1}{2}} = \frac{3(\phi^A)^n - (\phi^A)^{n-1}}{2}, (\check{\phi}^I)^{n+\frac{1}{2}} = \frac{3(\phi^I)^n - (\phi^I)^{n-1}}{2}, \\ (\phi^A)^{n+\frac{1}{2}} = \frac{(\phi^A)^n + (\phi^A)^{n+1}}{2}, (\phi^I)^{n+\frac{1}{2}} = \frac{(\phi^I)^n + (\phi^I)^{n+1}}{2}, \\ V_d((\phi^A)^n) = (h^A)^2 \sum_{i=1}^{N_x^A} \sum_{j=1}^{N_y^A} (\phi^A)_{ij}^n, V_d((\phi^I)^n) = (h^I)^2 \sum_{i=1}^{N_x^I} \sum_{j=1}^{N_y^I} (\phi^I)_{ij}^n, \\ (\omega^A)^n = -\frac{1}{2} \epsilon((\mathbf{u}^A)^n) : 3((\phi^A)^n)^2 \mathbf{D}^H : \epsilon((\mathbf{u}^A)^n), \\ (\omega^I)^n = -\frac{1}{2} \epsilon((\mathbf{u}^A)^n) : ((\phi^A)^{n+1})^3 \frac{\partial \mathbf{D}^H}{\partial (\phi^I)^n} : \epsilon((\mathbf{u}^A)^n), \\ \frac{\partial \mathbf{D}^H}{\partial (\phi^I)^n} = \frac{1}{|\Omega^I|} \sum_{i=1}^{N_x^I} \sum_{j=1}^{N_y^I} (\epsilon((\mathbf{u}^0)^n) - \epsilon((\mathbf{u}^I)^n)) : (3((\phi^I)_{ij}^n)^2) \mathbf{D}^I : (\epsilon((\mathbf{u}^0)^n) - \epsilon((\mathbf{u}^I)^n)). \end{cases} \tag{17}$$

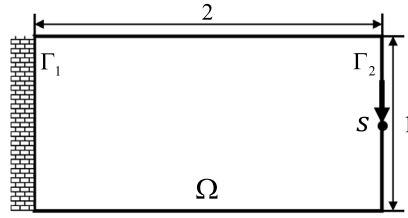


Fig. 5. The design domain for a cantilever beam.

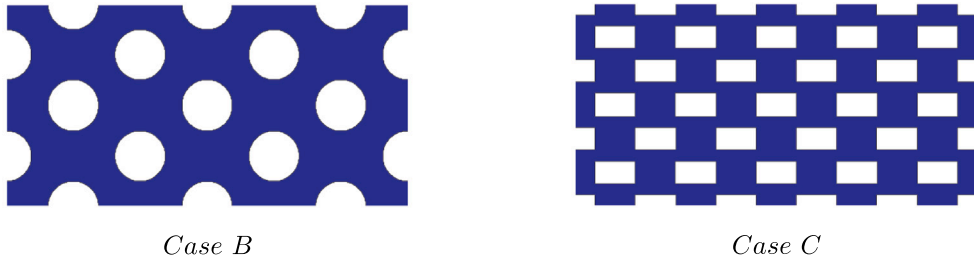


Fig. 6. The initial shape of Case B and Case C. (For interpretation of the references to color in this figure legend, the reader is referred to the web version of this article.)

Eqs. (16) and (17) are applied for the structures in which the periodical microstructures are considered for the infill region. When the microstructure of the infill region is not required, only Eqs. (6) need to be solved. In Section 4, shell-infill structures are designed to verify the effect of the present topology optimization framework in Section 2.3 and Section 2.4.

4. Numerical results

In this section, several numerical examples are provided to verify the effectiveness of the proposed phase field topology optimization method in the design of shell-infill structures. We perform a series of classical mechanical structures, and some of the parameters are set as follows unless otherwise specified: elasticity modulus $E = 1$, Poisson ratio $\nu = 0.3$, $g_{min} = 10^{-4}$, $\Delta t = 0.01$ in Eq. (13), $\Delta t^A = \Delta t^I = 0.01$ in Eq. (16), the stabilizing parameter $\lambda = 0.5$.

4.1. Shell-infill design of a cantilever beam

The first example is based on a cantilever beam, which is designed on a rectangular area with aspect ratio of 2:1. The design domain $\Omega = (0, 2) \times (0, 1)$ of the cantilever beam is demonstrated in Fig. 5. The left boundary Γ_1 is fixed, and a downward concentrated load is applied on the middle point of the right boundary Γ_2 . A uniform $N_x \times N_y = 512 \times 256$ rectangular mesh is applied to discretize the design domain. The width of the interface between solid and void region is chosen to $\epsilon = 5/(2\sqrt{2} \tanh^{-1}(0.9))$. The other parameters are set to $\eta = 4$ and $\beta = 50$.

Three different initial shapes are considered for the fundamental evolution to generate different based designs. For Case A, the solid material has the uniform distribution over the entire design domain, which means $\phi^0 = V_0 = 0.4$. For Case B, the initial solid material distribution contains several circle holes. For Case C, the initial solid material distribution contains rectangular holes. Fig. 6 shows the initial shape of Case B and Case C. The blue areas represent solid domain, and white areas represent void domain. The volume constrain for Case A, B and C is set to $V_0 = 0.4$.

With different initial shapes in different cases, the standard compliance minimization problem is respectively solved to obtain the based design. The based design ϕ_{Base} for different cases can be seen on the left of Fig. 7. The shell and infill region ϕ_{Shell} and ϕ_{Infill} are represented by ϕ_{Base} . The parameter to control the thickness of shell is set to $r_N = 1$. The infill region ϕ_{Infill} is optimized through the additional topology optimization process Eqs. (6) coupled with ϕ_{Shell} . The parameter g_1 is set to 0.6 for the material properties of the infill region, and the infill volume fraction is $V_1 = 0.75V_0$. The final structure Φ is obtained by the process of interpolation, which can be seen on the right of Fig. 7. In different cases, the shell-infill structures with porous infill structures are successfully obtained. Different initial shapes result in different based design, thus different cantilever beam structures with shell and porous infill can be designed.

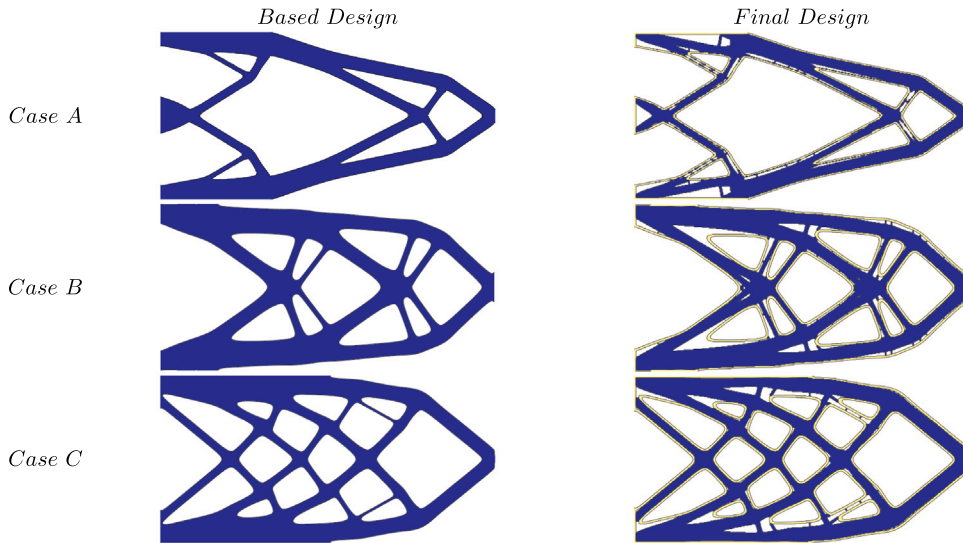


Fig. 7. The based design and the final shell-infill design for different initial shapes.

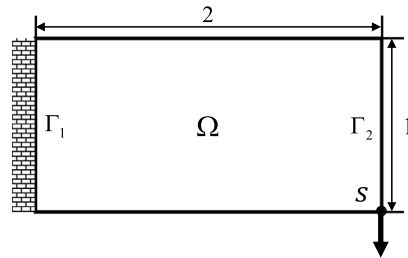


Fig. 8. The design domain for cantilever beam with a load at the lower right corner.

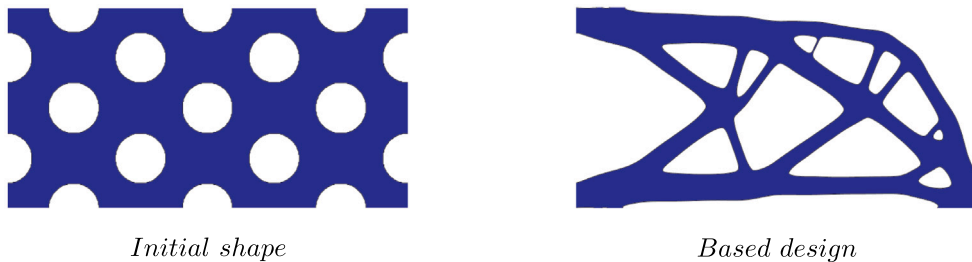


Fig. 9. The initial design and based design.

4.2. The effect of different design parameters

In Eqs. (6) and (9), g_1 and V_1 play an important role to determine the optimal shell-infill structures. The experiment targets in verifying the effect of these parameters through different comparison tests. The design domain for the cantilever beam is shown in Fig. 8, in which a concentrated load $s = (0, -1)$ is applied on the lower right corner. Using the same model parameters as Section 4.1, the initial design and the corresponding based design are shown in Fig. 9. In the first comparison test, the infill constrained volume fraction is given as $V_1 = 0.75V_0$, and different material property parameters $g_1 = 0.2, 0.4, 0.6$ are applied for the optimized shell-infill structures. In the second comparison test, the infill material property parameter $g_1 = 0.5$ keeps unchanged, and different constrained volume fraction $V_1 = 0.6V_0, 0.7V_0, 0.8V_0$ are used to obtain the final optimized shell-infill structures.

The results in Table 1 illustrate the different optimized shell-infill structures by the present method with different g_1 . The iteration histories of the compliance with different g_1 are also given here, as shown in Fig. 10. When different $g_1 = 0.2, 0.4$ and 0.6 are given, the compliance converge to 616, 312, and 215 respectively. Therefore we can see that larger g_1 results in the lower compliance. The

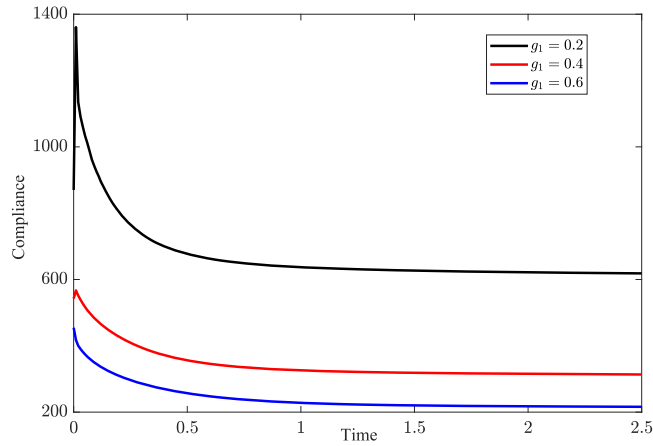


Fig. 10. The iteration histories of the compliance with different $g_1 = 0.2, 0.4, 0.6$.

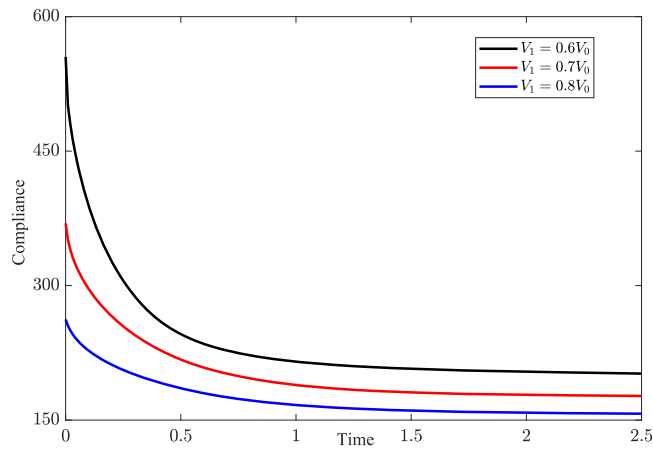


Fig. 11. The iteration histories of the compliance with different $V_1 = 0.6V_0, 0.7V_0, 0.8V_0$.

Table 1

The optimized layouts by the present method with different g_1 .

	$g_1 = 0.2$	$g_1 = 0.4$	$g_1 = 0.6$
$V_1 = 0.75V_0$			

Table 2

The optimized layouts by the present method with different V_1 .

	$V_1 = 0.6V_0$	$V_1 = 0.7V_0$	$V_1 = 0.8V_0$
$g_1 = 0.8$			

optimized shell-infill structures and the iteration histories of the compliance for the second comparison test are shown in Table 2 and Fig. 11, respectively. We can observe that with larger V_1 , the convergence values of compliance also reduce and the infill structures become denser.

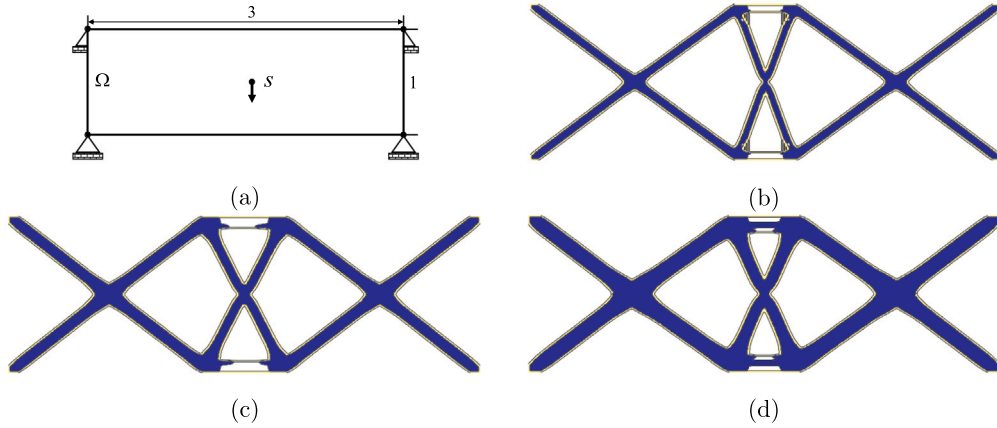


Fig. 12. (a) The design domain for a four-node fixed structure, and (b)-(d) the final design with different $V_0 = 0.5, 0.7$ and 0.9 , respectively.

4.3. Shell-infill design of a four-node fixed structure

The shell-infill design problem of a four-node fixed structure is investigated in this example. The design domain is discretized by 768×256 elements with aspect ratio $3 : 1$, which can be illustrated in Fig. 12(a). The four corners of the beam structure are fixed, and a concentrated load $s = (0, -1)$ is applied at the center point of the structure. Different volume fraction constraints $V_0 = 0.5, 0.7, 0.9$ are applied for the optimization of the based design ϕ_{Base} in Eq. (5), and different uniform initial solid material distributions $\phi^0 = V_0$ are used. The other parameters are kept for the design framework of shell-infill structures. The results can be seen in Fig. 12(b)-(d). As the initial volume constraint increases, the width of the beam structure correspondingly increases. Different shell-filling structures can be obtained by adjusting the initial volume fraction constraint.

4.4. Composite shell-infill design with different type TPMSs unit lattices

A triply periodic minimal surfaces (TPMS) is a surface on which the curvature of each point is equal to a constant and has periodic boundary conditions, and experiments has proven that TPMS is highly suitable for tissue scaffold. The structures using TPMSs unit lattices hold the advantage of high strength, energy absorption, exceptional lightweight and mechanical properties [50,51]. In this section, we perform the present single scale topology optimization method Eq. (6)-(7) in the composite shell-infill design with different type TPMSs unit lattices. We investigate the same shell-infill four-node fixed structure design problem as the situation with $V_0 = 0.7$ in Section 4.3. The infill region ϕ_{Infill} of the final shell-infill structure is redesigned by different type TPMSs unit lattices, in which TPMSs can be described implicitly [52]. The design results of composite shell-infill structures for the four-node fixed structures with different type TPMSs unit lattices can be indicated in Fig. 13. These results suggest that the present topology optimization method can successfully achieve the design of the composite shell-infill structures in the single macroscale, and the porous infill can be adjusted using different TPMSs.

4.5. Multi-scale shell-infill design

In this section, the shell-infill cantilever beam structures with different microstructures in the infill region are considered. The macro design domain is the same as that in Section 4.1. A rectangular mesh with size $N_x^A \times N_y^A = 512 \times 256$ and $h^A = 1/256$ is applied to discretize the macro design domain. The interface thickness ϵ^A is set to $5/(2\sqrt{2}\tanh^{-1}(0.9))$ in the macroscale. Other parameters for the macroscale evolution are chosen as $\eta^A = 4$ and $\beta^A = 50$. The volume constrain $V_0 = 0.8$. The based design ϕ_{Base} is first obtained through the standard topology optimization under the initial shape with circle holes. The initial shape and the based design are both shown in Fig. 14. We generate the shell region ϕ_{Shell} and the infill region ϕ_{Infill} from the based design. The shell region is fixed and the concurrent topology optimization is performed for ϕ_{Infill} . ϕ_{Infill} will be remained and used as the initial value of ϕ^A in Eqs. (16). The size of rectangular mesh for microscale is $L_x^I = L_y^I = 1/256$, $N_x^I = N_y^I = 64$ and $h^I = 1/(256 \times 64)$. The interface thickness for microscale is $\epsilon^I = 5/(2\sqrt{2}\tanh^{-1}(0.9))$. The other parameters for microscale are: $\eta^I = 4$ and $\beta^I = 50$.

In order to verify the effectiveness in different kinds of microstructures, different initial shapes of the micro phase field function are considered. Three microscale initial conditions are chosen:

$$(\phi^I)^0 = 2 \cos(2\pi x) \cos(2\pi y) - (\cos(4\pi x) + \cos(4\pi y)), \tag{18}$$

$$(\phi^I)^0 = 0.1 \cos(2\pi x) \cos(2\pi y) - (\cos(4\pi x) + \cos(4\pi y)), \tag{19}$$

$$(\phi^I)^0 = -\cos(4\pi x) \cos(4\pi y) - (\cos(4\pi x) + \cos(4\pi y)). \tag{20}$$

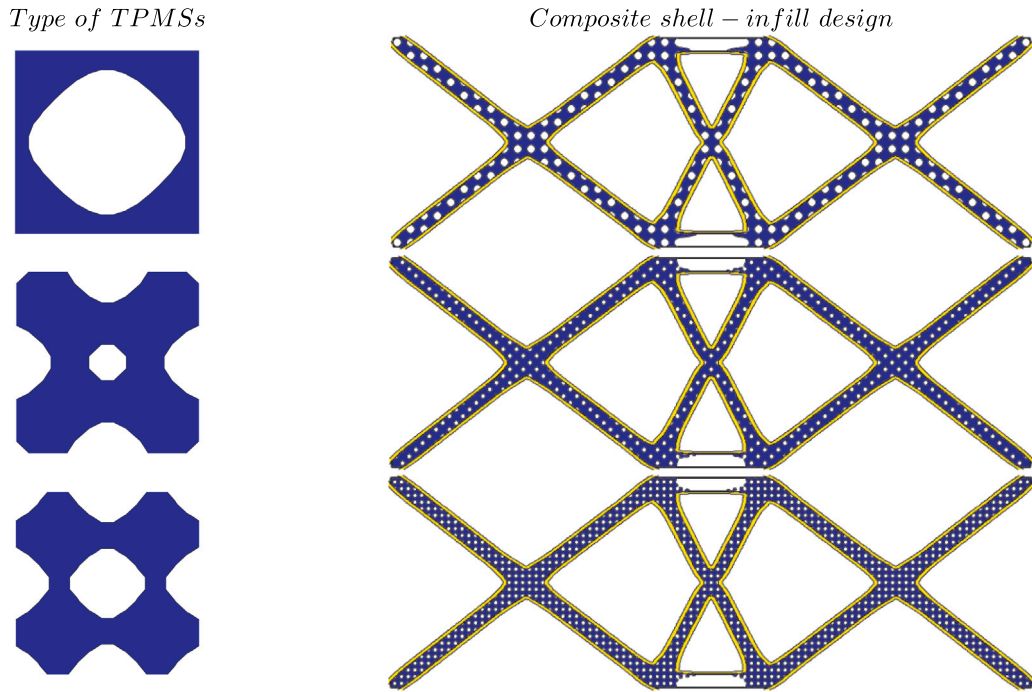


Fig. 13. The design results of composite shell-infill structures for the four-node fixed structures with different type TPMSs unit lattices.

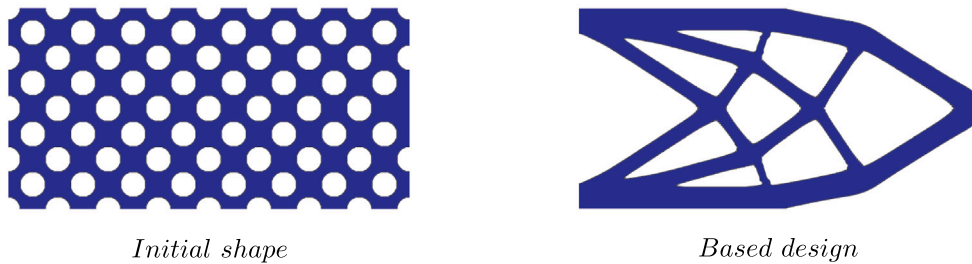


Fig. 14. The initial design and based design.

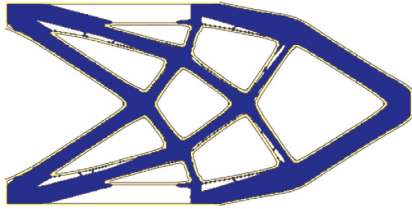
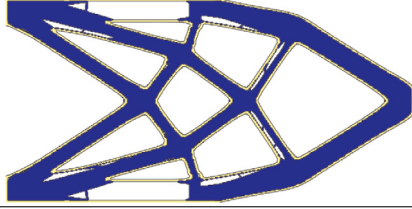
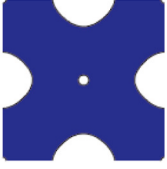
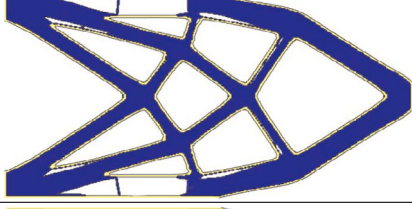

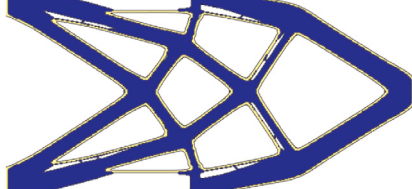

The material property parameter is chosen as $g_1 = 0.5$, and the volume constraint for infill region is set to $V_1 = 0.35V_0$ in Eqs. (9). The optimized shell-infill structures by the present method with different microstructures are shown in Table 3. In the first row of Table 3, the problem degrades to the shell-infill structures without the specific microstructure. The results in the second to fourth rows of Table 3 correspond to initial conditions Eqs. (18)–(20), respectively. The shell-infill structures based on the same based design are broadly similar. However, with different microstructures, the details of the optimized structure vary from each other, especially at the connection between the shell region and the infill region. Furthermore, when the microstructures change, the effective elasticity matrices \mathbf{D}^H through the numerical homogenization method are also different.

4.6. Shell-infill design of a bridge

In the section, we perform the example of shell-infill design for the bridge structure. 512×256 quadrilateral elements are used to discrete the design domain $\Omega = (0, 2) \times (0, 1)$. The left and right lower corners are fixed, and there is a concentrated load $\mathbf{s} = (0, -1)$ on the center of the bottom boundary, which is shown in Fig. 15. The initial shape and the result of the based design are shown in Fig. 16. Here the volume constrain of based design is $V_0 = 0.6$. Furthermore $V_1 = 0.35V_0$ and $g_1 = 0.5$. Different positive integers r_N are used to generate shell regions with different shell thicknesses.

The optimized shell-infill bridge structures with different $r_N = 1, 2, 3$ are shown in Fig. 17. In the present shell-infill representation strategy, the points belonging to the shell region are searched near the interface of the based design ϕ_{Base} . The control of the interface thickness is achieved by controlling the range of filtered points through the single parameter r_N . The phase field topology optimization method helps us to capture the solid-void interface quickly, thus enabling simple and fast shell region

Table 3
The optimized shell-infill structures by our method with different microstructures.

The optimized shell-infill structures	Microstructures	Homogenized elastic tensor
	None	None
		$\begin{bmatrix} 0.2590 & 0.0717 & 0.0000 \\ 0.0717 & 0.2350 & 0.0000 \\ 0.0000 & 0.0000 & 0.0760 \end{bmatrix}$
		$\begin{bmatrix} 0.1558 & 0.0179 & 0.0000 \\ 0.0179 & 0.1409 & 0.0000 \\ 0.0000 & 0.0000 & 0.0287 \end{bmatrix}$
		$\begin{bmatrix} 0.5270 & 0.1138 & 0.0000 \\ 0.1138 & 0.5058 & 0.0000 \\ 0.0000 & 0.0000 & 0.1315 \end{bmatrix}$

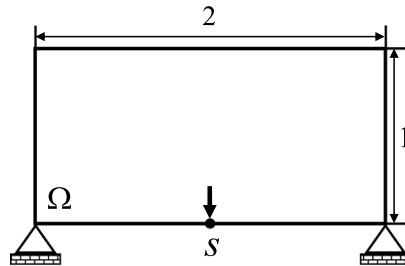


Fig. 15. The design domain for a bridge.

searching. The variation in thickness of the coated shell directly impacts the design considerations for infill structures. With larger r_N , the final structures have thicker solid shell, and thicker shell region leads to fewer porous areas in the infill region. Fig. 18 illustrates the iteration histories of the compliance with different shell thicknesses. When $r_N = 1, 2, 3$, the compliance of the shell-infill bridge structures converge to 447, 226, and 126 respectively. As the shell thickness parameter r_N increases, the infill becomes denser and the lower compliance is obtained.

Next the shell-infill bridge structures with specific microstructure are design at the case of $r_N = 3$. The initial condition for the microstructure is set as:

$$(\phi^I)^0 = (\cos(2\pi x) + \cos(2\pi y) + 2)/4.$$

Fig. 19(a) and (b) demonstrate the optimized shell-infill bridge structure and the final microstructure, respectively. Comparing Fig. 19(a) with the case of $r_N = 3$ in Fig. 17, the shell-infill bridge structure specific pattern of the microstructure contains more porous areas in the infill region.

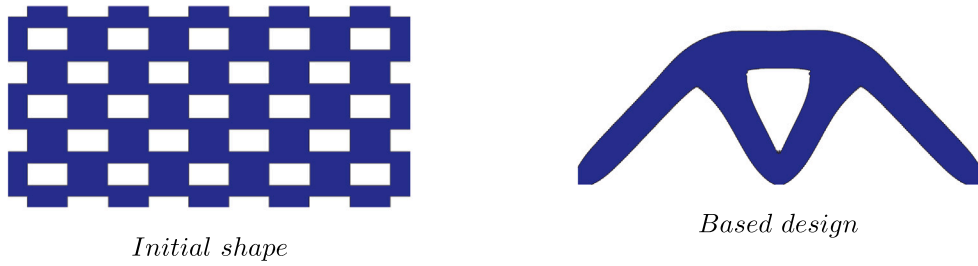


Fig. 16. The initial design and based design.

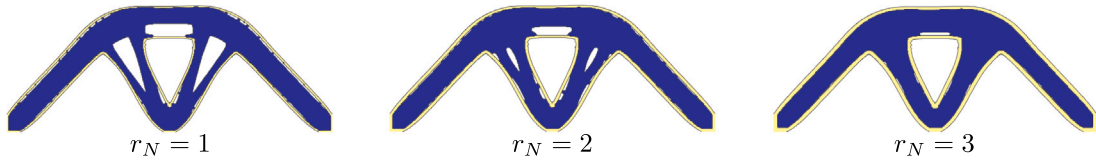


Fig. 17. The final design for different r_N .

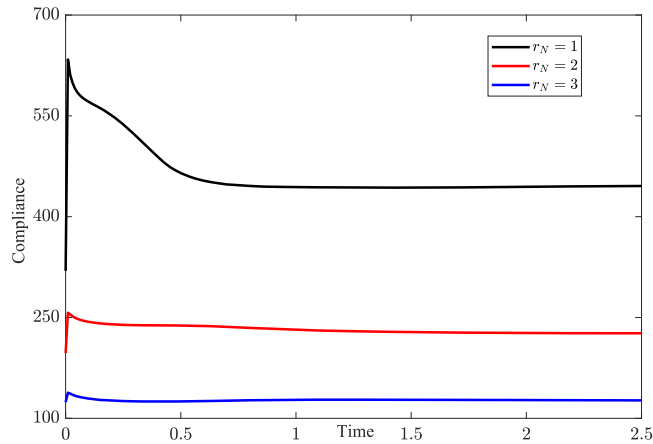


Fig. 18. The iteration histories of the compliance with different shell thicknesses $r_N = 1, 2, 3$.



Fig. 19. The optimized shell-infill structures(a) with final microstructures (b) when shell thickness $r_N = 3$.

4.7. Shell-infill design in three-dimension space

The final illustration pertains to a design challenge concerning 3D bridge-like structures, in which multiple load cases are considered. The dimensions and boundary conditions for this mechanical problem are presented in Fig. 20(a). Five vertical loads are applied individually at the top of the design domain. The design domain is discretized by a uniform $512 \times 256 \times 16$ quadrilateral elements. Fig. 20(b) illustrates the initial domain. The based structure is obtained with $\eta = 2, \beta = 5$ and $V_0 = 0.4$, which is shown

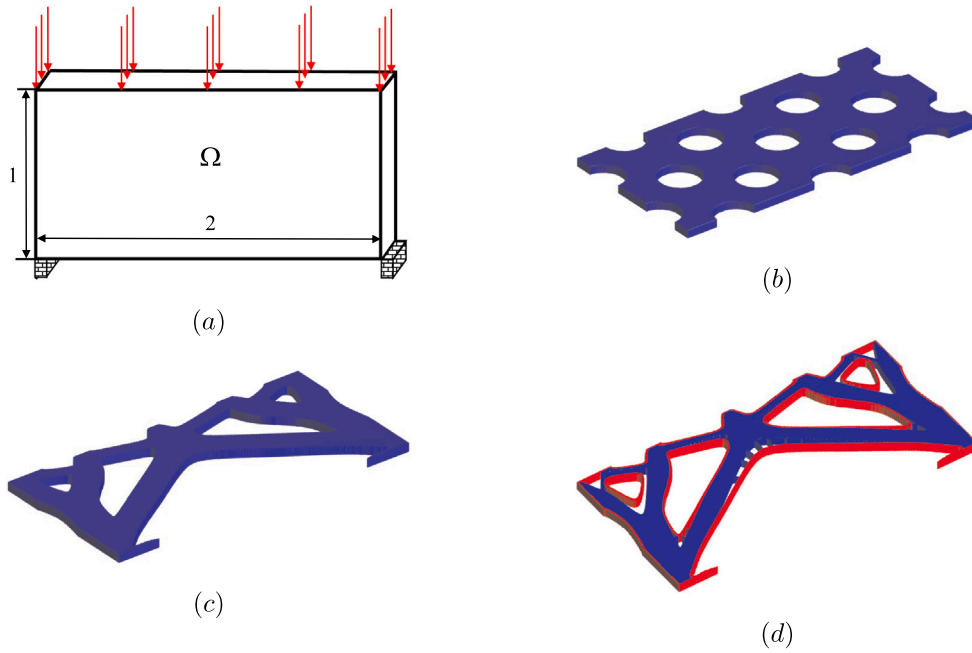


Fig. 20. The design of a 3D triangular-shaped (macro-)structures. (For interpretation of the references to color in this figure legend, the reader is referred to the web version of this article.)

in Fig. 20(c). Furthermore, $g_1 = 0.6$, $V_1 = 0.75V_0$ and $r_N = 1$ are chosen for the design of infill region. The optimized 3D shell-infill structures are given in Fig. 20(d). Here the red and blue colors are used to represent the shell and infill of the optimized structures. We note that the upper surface of the shell is not shown so that the structure of the infill region can be visualized directly. As can be seen, the proposed method can be naturally extended to the design of 3D shell-infill structures. Compared to the previous single load case problems, greater variations in the infill pattern can be seen in the results of multiple loads.

5. Conclusion

This paper introduced an innovative topology optimization method based on the phase field approach for the design of shell-infill structures. The utilization of the phase field function allowed for the natural identification of the interface, while providing a straightforward representation for both the shell and infill components. The porous infill could be obtained through a modified topology optimization, in which we specified different parameters to align the shell thickness, infill pattern and infill volume percentage, achieving a balance between cost and mechanical properties. The final shell-infill structures were obtained through the numerical interpolation scheme. Moreover, we addressed multiscale design considerations by applying the homogenization method to assess the effective elasticity matrix of the microstructural infill. Employing the multiscale phase field method facilitated the integration of microstructures with macroscale material properties, resulting in the uniform distribution of microstructures across the infill domain. Design examples of 2D and 3D shell-infill structures verified the effectiveness of the proposed framework.

CRedit authorship contribution statement

Wenxuan Xie: Writing – original draft, Visualization, Software, Methodology, Investigation, Conceptualization. **Jiachen Feng:** Writing – review & editing, Software, Conceptualization. **Qing Xia:** Writing – review & editing. **Junseok Kim:** Visualization, Methodology. **Yibao Li:** Writing – review & editing, Supervision, Software, Project administration, Methodology, Conceptualization.

Declaration of competing interest

The authors declared that they have no conflicts of interest to this work. We declare that we do not have any commercial or associative interest that represents a conflict of interest in connection with the work submitted.

Data availability

No data was used for the research described in the article.

Acknowledgments

This work is supported by National Natural Science Foundation of China (No. 12271430). The authors thank the reviewers for the constructive and helpful comments on the revision of this article.

References

- [1] J. Fu, H. Li, L. Gao, M. Xiao, Design of shell-infill structures by a multiscale level set topology optimization method, *Comput. Struct.* 212 (2019) 162–172.
- [2] A. Mitchell, U. Lafont, M. Holyńska, C. Semprinoschnig, Additive manufacturing - A review of 4D printing and future applications, *Addit. Manuf.* 24 (2018) 606–626.
- [3] A. Plessis, C. Broeckhoven, I. Yadroitsava, I. Yadroitsev, C.H. Hands, R. Kunju, D. Bhate, Beautiful and functional: A. Review of biomimetic design in additive manufacturing, *Addit. Manuf.* 27 (2019) 408–427.
- [4] X. Chen, C. Li, Y. Bai, Topology optimization of sandwich structures with solid-porous hybrid infill under geometric constraints, *Comput. Methods Appl. Mech. Engrg.* 382 (2021) 113856.
- [5] J. Hu, Y. Luo, S. Liu, Two-scale concurrent topology optimization method of hierarchical structures with self-connected multiple lattice-material domains, *Compos. Struct.* 272 (2021) 114224.
- [6] S. Chu, L. Gao, M. Xiao, H. Li, Design of sandwich panels with truss cores using explicit topology optimization, *Compos. Struct.* 210 (2019) 892–905.
- [7] Y. Liu, Z. Lai, Y. Lu, M. Zhou, Z. Lin, Topology optimization of shell-infill structures considering buckling constraint, *Comput. Struct.* 283 (2023) 107055.
- [8] A. Clausen, N. Aage, O. Sigmund, Exploiting additive manufacturing infill in topology optimization for improved buckling load, *Engineering 2* (2016) 250–257.
- [9] M.P. Bendsøe, N. Kikuchi, Generating optimal topologies in structural design using a homogenization method, *Comput. Methods Appl. Mech. Engrg.* 71 (1999) 197–224.
- [10] O. Sigmund, K. Maute, Topology optimization approaches, *Struct. Multidiscip. Optim.* 48 (2013) 1031–1055.
- [11] M.P. Bendsøe, Optimal shape design as a material distribution problem, *Struct. Optim.* 1 (1989) 193–202.
- [12] A. Clausen, N. Aage, O. Sigmund, Topology optimization of coated structures and material interface problems, *Comput. Methods Appl. Mech. Engrg.* 290 (2015) 524–541.
- [13] A. Clausen, E. Andreassen, O. Sigmund, Topology optimization of 3D shell structures with porous infill, *Acta Mech. Sin.* 33 (4) (2017) 778–791.
- [14] J. Wu, N. Aage, R. Westermann, O. Sigmund, Infill optimization for additive manufacturing –approaching bone-like porous structures, *IEEE Trans. Vis. Comput. Graphics* 99 (2017) 1–14.
- [15] J. Wu, A. Clausen, O. Sigmund, Minimum compliance topology optimization of shell-infill composites for additive manufacturing, *Comput. Methods Appl. Mech. Engrg.* 326 (2017) 358–375.
- [16] M. Zhou, Y. Lu, Y. Liu, Z. Lin, Concurrent topology optimization of shells with self-supporting infills for additive manufacturing, *Comput. Methods Appl. Mech. Engrg.* 390 (2022) 114430.
- [17] Y. Luo, Q. Li, S. Liu, Topology optimization of shell-infill structures using an erosion-based interface identification method, *Comput. Methods Appl. Mech. Engrg.* 355 (2019) 94–112.
- [18] W. Qiu, P. Jin, S. Jin, C. Wang, L. Xia, J. Zhu, T. Shi, An evolutionary design approach to shell-infill structures, *Addit. Manuf.* 34 (2020) 101382.
- [19] L. Xia, Q. Xia, X. Huang, Y.M. Xie, Bi-directional evolutionary structural optimization on advanced structures and materials: A comprehensive review, *Arch. Comput. Methods Eng.* 25 (2018) 437–478.
- [20] A.R. Diaz, O. Sigmund, Checkerboard patterns in layout optimization, *Struct. Optim.* 10 (1995) 40–45.
- [21] Y. Wang, Z. Kang, A level set method for shape and topology optimization of coated structures, *Comput. Methods Appl. Mech. Engrg.* 329 (2018) 553–574.
- [22] J. Bai, W. Zuo, Multi-material topology optimization of coated structures using level set method, *Compos. Struct.* 300 (2022) 116074.
- [23] A. Takezawa, S. Nishiwaki, M. Kitamura, Shape and topology optimization based on the phase field method and sensitivity analysis, *J. Comput. Phys.* 229 (2010) 2697–2718.
- [24] P.H. Chiu, Y.T. Lin, A conservative phase field method for solving incompressible two-phase flows, *J. Comput. Phys.* 230 (2011) 185–204.
- [25] Q. Yu, K. Wang, B. Xia, Y. Li, First and second order unconditionally energy stable schemes for topology optimization based on phase field method, *Appl. Math. Comput.* 405 (2021) 126267.
- [26] Q. Yu, Y. Li, A second-order unconditionally energy stable scheme for phase-field based multimaterial topology optimization, *Comput. Methods Appl. Mech. Engrg.* 405 (2023) 115876.
- [27] Q. Xia, G. Sun, Q. Yu, J. Kim, Y. Li, Thermal-fluid topology optimization with unconditional energy stability and second-order accuracy via phase-field model, *Commun. Nonlinear Sci. Numer. Simul.* 116 (2023) 106782.
- [28] Y. Li, K. Wang, Q. Yu, Q. Xia, J. Kim, Unconditionally energy stable schemes for fluid-based topology optimization, *Commun. Nonlinear Sci. Numer. Simul.* 111 (2022) 106433.
- [29] W. Xie, Q. Xia, Q. Yu, Y. Li, An effective phase field method for topology optimization without the curvature effects, *Comput. Math. Appl.* 146 (2023) 200–212.
- [30] P.H. Chiu, Y.T. Lin, A conservative phase field method for solving incompressible two-phase flows, *J. Comput. Phys.* 230 (2011) 185–204.
- [31] J. Fu, H. Li, L. Gao, M. Xiao, Design of shell-infill structures by a multiscale level set topology optimization method, *Comput. Struct.* 212 (2019) 162–172.
- [32] J. Groen, J. Wu, O. Sigmund, Homogenization-based stiffness optimization and projection of 2D coated structures with orthotropic infill, *Comput. Methods Appl. Mech. Engrg.* 349 (2019) 722–742.
- [33] J. Lee, C. Kwon, J. Yoo, S. Min, T. Nomura, E. Dede, Design of spatially-varying orthotropic infill structures using multiscale topology optimization and explicit de-homogenization, *Addit. Manuf.* 40 (2021) 101920.
- [34] J. Gao, Z. Luo, H. Li, P. Li, L. Gao, Dynamic multiscale topology optimization for multi-regional microstructured cellular composites, *Compos. Struct.* 211 (2019) 401–417.
- [35] J. Gao, Z. Luo, L. Xia, L. Gao, Concurrent topology optimization of multiscale composite structures in matlab, *Struct. Multidiscip. Optim.* 60 (2019) 2621–2651.
- [36] J. Gao, Z. Luo, H. Li, L. Gao, Topology optimization for multiscale design of porous composites with multi-domain microstructures, *Comput. Methods Appl. Mech. Engrg.* 344 (2019) 451–476.
- [37] E. Wadbro, B. Niu, Multiscale design for additive manufactured structures with solid coating and periodic infill pattern, *Comput. Methods Appl. Mech. Engrg.* 357 (2019) 112605.
- [38] S. Xu, J. Liu, J. Huang, B. Zou, Y. Ma, Multi-scale topology optimization with shell and interface layers for additive manufacturing, *Addit. Manuf.* 37 (2021) 101698.
- [39] Q. Yu, Q. Xia, Y. Li, A phase field-based systematic multiscale topology optimization method for porous structures design, *J. Comput. Phys.* 466 (2022) 111383.
- [40] C. Wang, S. Wise, A thermodynamically-consistent phase field crystal model of solidification with heat flux, *J. Math. Study* 55 (2022) 337–357.

- [41] D. Wang, An efficient unconditionally stable method for dirichlet partitions in arbitrary domains, 2021, pp. 1–27, arXiv preprint arXiv:2108.11552.
- [42] W. Xie, Y. Li, A novel estimation method for microstructural evolution based on data assimilation and phase field crystal model, *Commun. Nonlinear Sci. Numer. Simul.* 127 (2023) 107562.
- [43] L. Xia, P. Breitkopf, Design of materials using topology optimization and energybased homogenization approach in matlab, *Struct. Multidiscip. Optim.* 52 (2015) 1229–1241.
- [44] S. Chu, L. Gao, M. Xiao, Y. Zhang, Multiscale topology optimization for coated structures with multifarious-microstructural infill, *Struct. Multidiscip. Optim.* 61 (2020) 1473–1494.
- [45] M. Wang, Q. Huang, C. Wang, A second order accurate scalar auxiliary variable (SAV) numerical method for the square phase field crystal equation, *J. Sci. Comput.* 88 (2021) 1–36.
- [46] D. Wang, B. Osting, X. Wang, Interface dynamics for an Allen-Cahn-type equation governing a matrix-valued field, *Multiscale Model. Simul.* 17 (2019) 1252–1273.
- [47] J. Yang, J. Kim, A phase-field model and its efficient numerical method for two-phase flows on arbitrarily curved surfaces in 3D space, *Comput. Methods Appl. Mech. Engrg.* 372 (2020) 113382.
- [48] J. Kim, A numerical method for the cahn-hilliard equation with a variable mobility, *Commun. Nonlinear Sci. Numer. Simul.* 12 (2007) 1560–1571.
- [49] U. Trottenberg, C. Oosterlee, A. Schüller, *Multigrid*, Academic Press, USA, 2001.
- [50] Y. Li, Q. Xia, S. Kang, S. Kwak, J. Kim, A practical algorithm for the design of multiple-sized porous scaffolds with triply periodic structures, *Math. Comput. Simulation* 220 (2024) 481–495.
- [51] D. Abueidda, M. Bakir, R. Al-Rub, J. Bergstrom, N. Sobh, I. Jasiuk, Mechanical properties of 3D printed polymeric cellular materials with triply periodic minimal surface architectures, *Mater. Des.* 122 (2017) 255–267.
- [52] Y. Li, Q. Xia, S. Yoon, C. Lee, B. Lu, J. Kim, A simple and efficient volume merging method for triply periodic minimal structure, *Comput. Phys. Comm.* 264 (2021) 107956.